Available online at www.sciencedirect.com

jmr&t
Journal of Materials Research and Technology

journal homepage: www.elsevier.com/locate/jmrt

Original Article

Enhanced pseudoelasticity of an Fe–Mn–Si-based shape memory alloy by applying microstructural engineering through recrystallization and precipitation

Hesamodin Khodaverdi [a], *Maryam Mohri* [b,**], *Elyas Ghafoori* [b,c], *Amir Sabet Ghorabaei* [a], *Mahmoud Nili-Ahmadabadi* [a,*]

[a] *School of Metallurgy and Materials Engineering, College of Engineering, University of Tehran, Tehran, Iran*
[b] *Empa, Swiss Federal Laboratories for Materials Science and Technology, 8600 Dübendorf, Switzerland*
[c] *Institute for Steel Construction, Faculty of Civil Engineering and Geodetic Science, Leibniz University Hannover, 30167 Hannover, Germany*

ARTICLE INFO

Article history:
Received 9 August 2022
Accepted 19 October 2022
Available online 29 October 2022

Keywords:
Fe–17Mn–5Si–10Cr–4Ni–1(V–C) (wt.%)
Fe-based shape memory alloy (SMA)
Superelasticity
Residual strain
Grain refinement

ABSTRACT

The aim of this work is to provide a novel understanding of pseudoelasticity mechanisms in an FeMnSi-based shape memory alloy and to utilize the identified parameters to control and enhance the mechanical behavior of the alloy. The alloy was processed by employing caliber rolling to an equivalent strain of 0.25 at room temperature. Various heat treatments from 530 to 1000 °C were applied to study the microstructural evolution and pseudoelasticity behavior during short-term post-deformation annealing (PDA) and aging. A minimum residual strain of 2.85% was achieved after 4% loading in tension by annealing the cold-worked sample at 925 °C for 50 min followed by aging at 750 °C for 6 h; this is the lowest ever reported residual strain for this alloy. Moreover, the absorbed energy increased from 17 to 22 J/cm^3, indicating a 30% enhancement compared with the as-received aged sample. These improvements in pseudoelasticity and absorbed energy make this alloy more suitable for seismic damping application by providing more recentering after energy dissipation. The improvements are mainly attributed to grain refinement, which stimulates a uniform distribution of precipitates inside the austenite grains after PDA and aging. Additionally, grain refinement modifies the morphology and size of precipitates, resulting in an increased number of stacking faults and a high volume fraction of ε-martensite, and diminishes the probability of the intersection of ε-martensite laths with each other and subsequent α′-martensite formation.

© 2022 The Author(s). Published by Elsevier B.V. This is an open access article under the CC BY-NC-ND license (http://creativecommons.org/licenses/by-nc-nd/4.0/).

* Corresponding author.
** Corresponding author.
E-mail addresses: maryam.mohri@empa.ch (M. Mohri), nili@ut.ac.ir (M. Nili-Ahmadabadi).
https://doi.org/10.1016/j.jmrt.2022.10.092
2238-7854/© 2022 The Author(s). Published by Elsevier B.V. This is an open access article under the CC BY-NC-ND license (http://creativecommons.org/licenses/by-nc-nd/4.0/).

1. Introduction

Most studies on the applications of shape memory alloys (SMAs) have been conducted by using Ni–Ti SMA (Nitinol) alloys, which are the most renowned and readily available SMAs [1]. Nitinol alloys show a significant reversible strain because of unloading (pseudoelasticity (PE)) or heating (shape memory effect) and have been used for many applications in medical and aerospace engineering [2,3]. However, applications of Nitinol in large civil structures have been restricted owing to the high cost of raw materials and processing routes, hard formability, narrow thermal hysteresis, and low damping capacity (absorbed or dissipated energy) [4]. Moreover, research on seismic damping alloys indicates that the absorbed energy during deformation and the PE of SMAs are vital for improving the structural behavior in an earthquake. In addition to the high capacity for absorbing earthquake energy, the minimum residual deformation after unloading should be considered [5].

Fe-based SMAs (Fe-SMAs), such as Fe–Mn–Si-based SMAs, are an alternative to Nitinol and have more advantages for large-scale applications in the construction sector. These characteristics include low material costs, high elastic stiffness and strength, wide thermal transformation hysteresis [6], exceptional workability [7], good weldability and machinability [8], and defensible stress and strain recovery [9]. Recently, Fe–Mn–Si-based SMAs have been considered for various structural applications, such as coupling devices, mechanical tightening, structural elements [8,10], active control [11], pre-stressing or post-tensioning of structures [12], and damping devices [13] in civil engineering. Despite the aforementioned attributes, Fe–Mn–Si alloys have low PE, which restricts their seismic applications [14].

The PE of Fe–Mn–Si-based SMAs is a result of reverse transformation from ϵ-martensite with hexagonal close-packed (HCP) crystal structure to γ-austenite with face-centered cubic (FCC) crystal structure by backward movement of the leading partial dislocation in the FCC crystal [15]. The PE depends on processing parameters, such as deformation temperature and total strain, and material parameters, such as stacking fault energy (SFE), grain size, texture, and precipitates (volume fraction, size, shape, and distribution). Strain-induced martensitic transformation occurs when the SFE is typically lower than a threshold value. When the SFE is greater than 40 mJ/m^2, dislocation slip occurs after the elastic deformation of the parent austenite phase, causing plastic deformation. Mechanical twinning and stress-induced martensitic transformation occur if the SFE is in the range of 20–40 mJ/m^2 and less than 20 mJ/m^2, respectively [16]. Furthermore, decreasing the average grain size of the austenitic matrix increases the PE, which is explained by the effect of the growing amount of grain boundaries on increasing the exertion of back stresses on the tip of the HCP bands [17]. Moreover, the strength of the parent phase is enhanced by decreasing the average grain size; thus, the plastic deformation by twinning or slip is minimized, enabling the $\gamma \rightleftharpoons \varepsilon$ transformation and, consequently, PE promotion [18].

The PE also increases by inducing a fine dispersion of nano-sized precipitates, such as NbC, VC, and VN, in the austenite phase. NbC precipitates strengthen the γ-phase and assist in the reversible movement of γ/ε interfaces through a specific crystallographic path. Such behavior partly results from the back stress on the growing ϵ-martensite lath caused by the coherent stress fields of the NbC carbides [19,20]. VN precipitates promote the number of dislocations and stacking faults (SFs) in the microstructure. The precipitates and SFs enhance both the formation of ε-martensite during pre-straining and the reverse $\varepsilon \rightarrow \gamma$ transformation during unloading [21].

A new design for Fe-SMAs with finely dispersed VC particles, Fe–17Mn–5Si–10Cr–4Ni–1(V–C) (wt.%), has recently been developed at the Swiss Federal Laboratories for Materials Science and Technology (Empa). The alloy can be produced by using an inexpensive manufacturing casting process under atmospheric conditions [6] and can generate a high recovery stress of approximately 448 MPa after pre-straining to 8% and heating to a temperature of 455 °C without any high-cost "training" processing [9]. The alloy has exhibited a high potential for large-scale repair and strengthening in the construction section [22] and passive vibration damping [23]. Many studies have been conducted on the recovery stress behavior [9,24,25], low-cycle fatigue [26], high-cycle fatigue [27], elevated-temperature behavior [28], bonding ability [29], and additive manufacturing [30] of Fe–Mn–Si-based SMAs. This material has been used for large-scale bridge girders, connections [31,32], and plates [33–35]. Although the alloy shows a very good shape memory effect, it suffers from low PE [17]. Any improvement in the alloy's PE will result in a further increase in its potential for recentering and energy dissipation applications in the construction sector. Therefore, the aim of this work is to investigate the effect of different thermo-mechanical treatments on the PE response of the alloy.

2. Materials and methods

The as-received alloy used in this study was an 18 mm Ø rebar R18 with a nominal composition of Fe–17Mn–5Si–10Cr–4Ni–1(V–C) (wt.%) provided by re-fer AG, Switzerland. The rebar was produced by hot rolling at 1000 °C after casting. The as-received sample was then cold–caliber-rolled to an octagonal-shaped specimen with equal sides of 14.2 mm at ambient temperature by using a caliber rolling machine with a roller diameter of 110 mm to achieve an equivalent strain of 0.25 after 16 rolling passes. The rolling speed was set at 800 mm/min. The cold-caliber-rolled specimens were recrystallized in a vacuum furnace at various temperatures and times. Aging was performed at 750 °C under atmospheric conditions for 6 h followed by air cooling to the ambient temperature. All heat treatment conditions are listed in Table 1.

The phase constituents were determined using X-ray diffraction (XRD) with Cu Kα radiation (wavelength $\lambda = 0.154$ nm) at 45 kV and a tube current of 200 mA. Cylindrical samples having a length of 10 mm and a diameter of up to 2 mm were cut and inserted in an Adamel DT1000 dilatometer to conduct a thermal study on the cold-worked sample. Microstructural characterization was performed by optical microscopy (OM; ZEISS Axioskop 2 MAT), field-emission scanning electron microscopy (FE-SEM; FEI Nova NanoSEM 450), and high-resolution transmission electron

Table 1 – List of heat treatments. R. Temperature: recrystallization temperature; R. Time: recrystallization time.

Name	Cold worked	R. Temperature (°C)	R. Time (min)	Aged (750 °C-6 h)
As-received	–	–	–	–
As-received aged	–	–	–	✓
Cold-worked	✓	–	–	–
Anneal-530	✓	530	120	–
Anneal-630	✓	630	120	–
Anneal-750	✓	750	120	–
Rex925	✓	925	50	–
Rex950	✓	950	50	–
Rex900-aged	✓	900	50	✓
Rex925-aged	✓	925	50	✓
Rex950-aged	✓	950	50	✓
Rex980-aged	✓	980	50	✓
Rex1000-aged	✓	1000	10	✓

microscopy (HR-TEM; FEI Tecnai F20 series). Local area chemical compositions were analyzed by energy-dispersive X-ray spectroscopy (EDS; Oxford X-Max^N detector) in the TEM. Samples for the OM and SEM observations were polished and etched with a solution of H_2O_2 (35%), HNO_3 (65%), and HCl (32%) (7:30:9). The HR-TEM specimens were prepared by employing standard mechanical thinning and electro-polishing. The electrolyte was a solution of $HClO_4$ and C_2H_5OH (1:9) at −20 °C and 22 V.

To investigate the evolution of the mechanical properties as a microstructure function, monotonic loading–unloading experiments were performed by using a Zwick/Roell Z020 tensile test machine. Longitudinal tensile specimens were machined from the samples and prepared in a dog-bone shape with a reduced section length of 32 mm and a cross-section of 1 × 0.8 mm^2 (Fig. 1). Loading to 4% strain was performed at room temperature with a crosshead speed of 0.5 mm/min followed by unloading with the same crosshead speed until a force of 10 N was reached. The strain hardening exponent (n) was calculated by plotting ln(σ) vs. ln(ε) in the nonlinear part of loading and then measuring the slope of the resultant curve.

3. Results

The SFE value was calculated to be 5.75 mJ/m^2, using the equation provided by Li et al. [36]. A low SFE value increases the probability of strain-induced ε-martensitic transformation, rather than dislocation slip or twinning [16]. The low SFE value suggests a good PE potential for this alloy after microstructural engineering.

3.1. *Thermal analysis and microstructural development*

Isochronal analysis was conducted using dilatometry to study the microstructural evolution during post-deformation annealing. The corresponding curves for the as-received and cold-worked samples are shown in Fig. 2. The curve of the as-received sample showed a smooth deviation from the linear curve (420–560 °C). This phenomenon will be investigated and reported in a future publication. The related curve of the as-received sample showed another smooth deviation from the linear curve (680–800 °C) related to (Cr–V)-rich carbide formation [37]. Furthermore, in the curve of the cold-worked sample, an intense slope change started at 505 °C and ended at 750 °C, and a slight change in the slope at 875 °C was observed.

Fig. 3 shows the optical micrographs of the as-received (a), as-received aged (b), cold-worked (c), Anneal-530 (d), Anneal-630 (e), and Anneal-750 (f) samples. Annealing temperatures were selected according to the slope change range in the dilatometry analysis. The optical microscopy microstructure of the as-received sample contained precipitate-free equiaxed grains, with a mean grain size of 14 μm. After annealing was performed for 6 h, some austenite grains experienced grain growth, and consequently, the mean grain size reached 17 μm with a more non-uniform size distribution of grains. The micrograph of the cold-worked sample showed a typical deformed microstructure containing elongated grains. The morphologies of the grains after cold working and annealing at 530 °C, 630 °C, and 750 °C for 2 h were similar to those of the cold-worked sample; the elongated grains remained unchanged. These observations indicated that recrystallization due to annealing did not occur below 750 °C in the cold-worked samples, but the grains were occupied by tangled lines that could be twin bands, slip bands, or HCP martensite bands, which are typical of cold-worked and annealed austenitic steels [38].

Fig. 4 shows the optical micrographs of the samples recrystallized at temperatures above 900 °C. In contrast to the

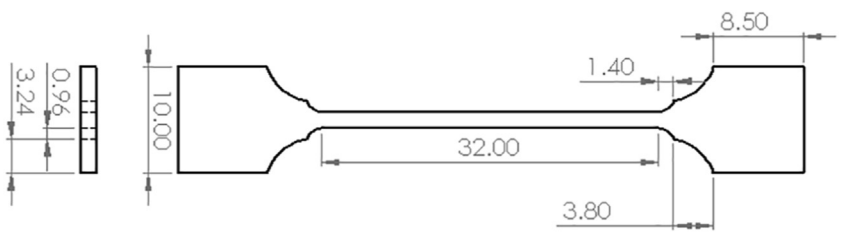

Fig. 1 – Geometry of the dog-bone specimens used for the tensile tests (dimensions in mm).

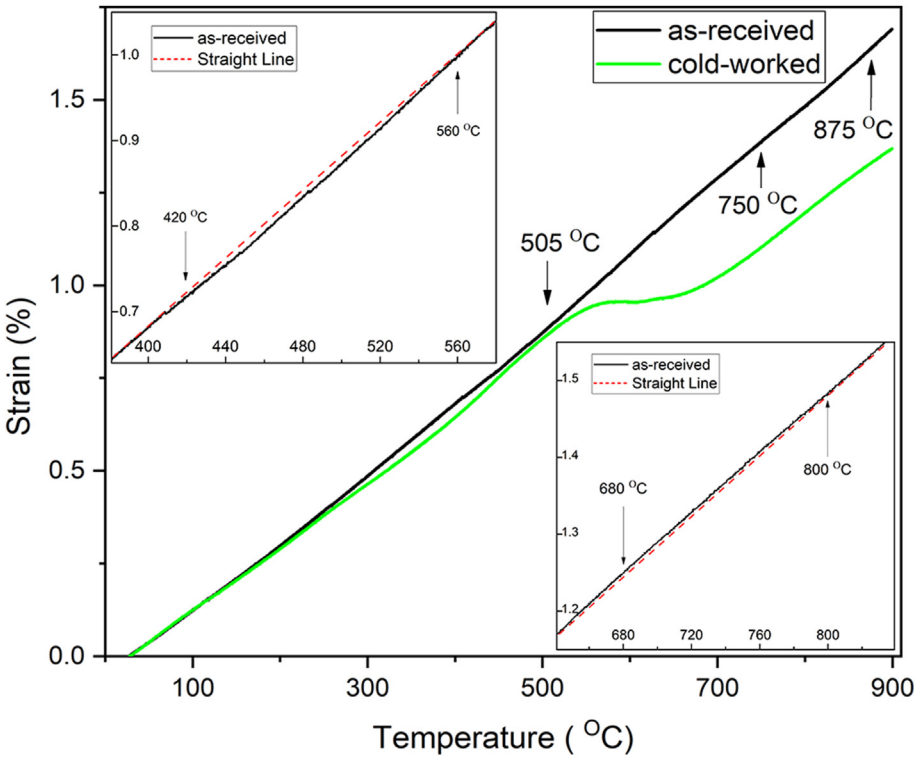

Fig. 2 – Dilatation curves versus temperature at the heating rate of 3 °C/min for the as-received and cold-worked specimens.

samples annealed at 530–750 °C (Fig. 3d–f), the microstructure of the samples contained rejuvenated grains that were free from tangled lines (Fig. 4). The grain boundaries in the aged samples (Fig. 4b–f) were more easily detectable than those of the unaged sample (Fig. 4a). The aged sample after annealing at 900 °C (Fig. 4b) did not exhibit a fully recrystallized microstructure, indicating that annealing for 50 min at 900 °C was insufficient to achieve complete recrystallization in this sample. However, the Rex925-aged sample (Fig. 4c) showed equiaxed grains with a mean grain size of 5 μm and an almost uniform size distribution, whereas abnormal grain growth occurred in the samples annealed at higher temperatures.

The microstructural features are revealed in the FE-SEM micrographs of the samples as shown in Fig. 5. The microstructure of the as-received sample (Fig. 5a) showed needle-shaped and polyhedral-shaped precipitates elongated at the grain boundaries with 250–650 nm length, but no precipitate

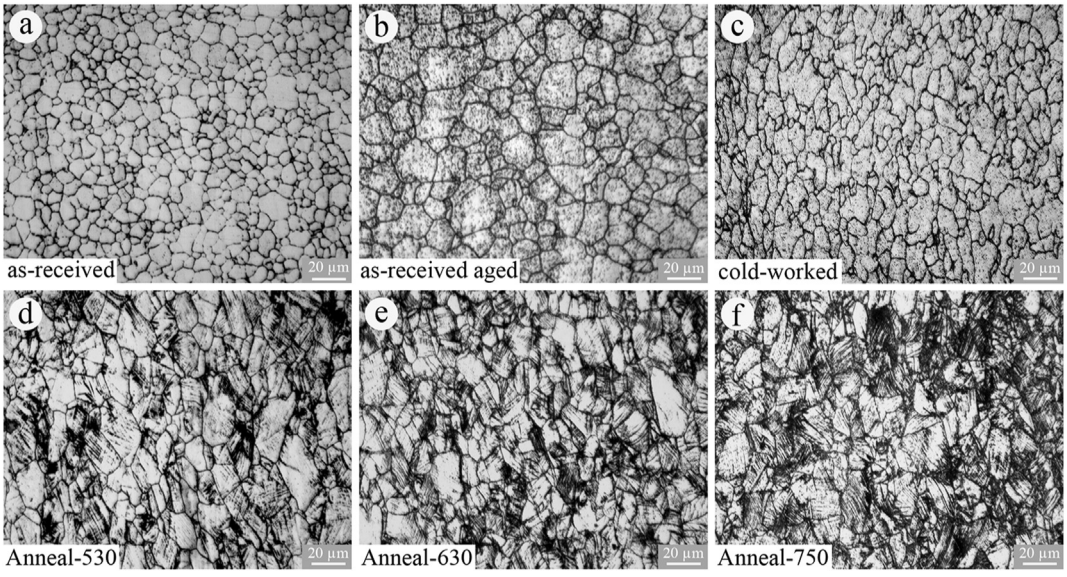

Fig. 3 – OM microstructure of the (a) as-received, (b) as-received aged, (c) cold-worked, (d) Anneal-530, (e) Anneal-630, and (f) Anneal-750 samples.

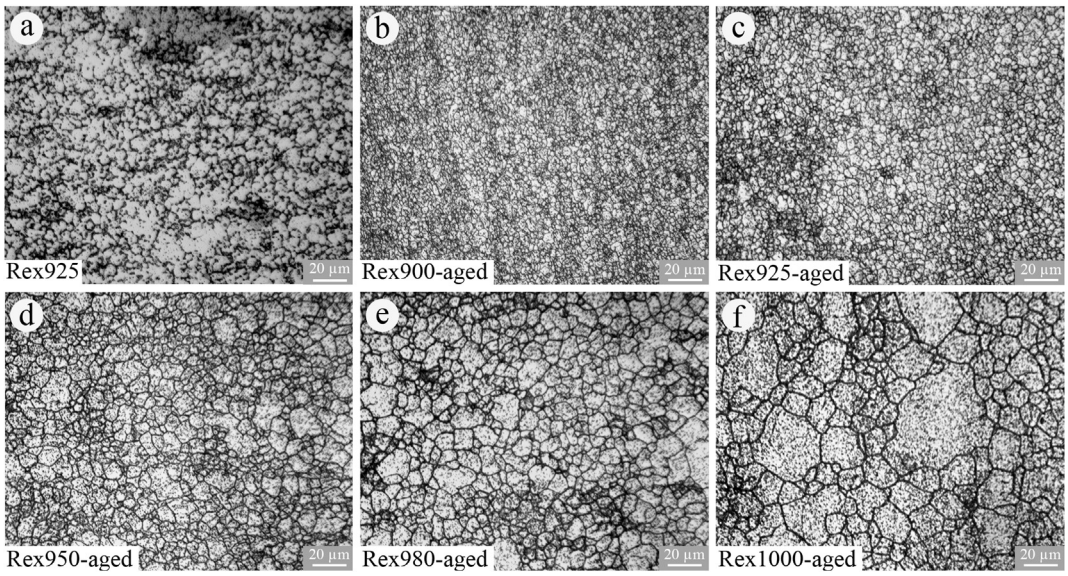

Fig. 4 – OM microstructure of the (a) Rex925, (b) Rex900-aged, (c) Rex925-aged, (d) Rex950-aged, (e) Rex980-aged, and (f) Rex1000-aged samples.

was observed inside the grains. The as-received sample after aging at 750 °C for 6 h (Fig. 5b) showed a sharp increase in the number of precipitates at the grain boundaries with almost similar morphology but coarser than the as-received sample precipitates. There were two types of precipitates inside the grains: polyhedral- and bar-shaped, although the number of precipitates at the grain boundaries was much greater than that in the grain interior. Additionally, by performing aging heat treatment, the average grain size increased from 14 μm to 17 μm. Annealing of the cold-worked sample at 925 °C for 50 min (Fig. 5c) resulted in recrystallization, reducing the average grain size to 5 μm. SEM-EDS analysis accompanied by TEM studies showed that the bright areas with a diameter of approximately 1 μm (usually in triple junctions) were austenite grains, while the bright areas with smaller sizes of less than 800 nm and within the grain boundaries were precipitates (see Section 3.3). After recrystallization, the sample was aged at 750 °C for 6 h (Fig. 5d). Unlike the as-received aged sample, the Rex925-aged sample exhibited a sharp increase in the number of precipitates inside the grains with a higher volume fraction than that of the grain boundary precipitates. The precipitates had a more uniform distribution within the microstructure of the Rex925-aged sample in comparison to the as-received aged sample.

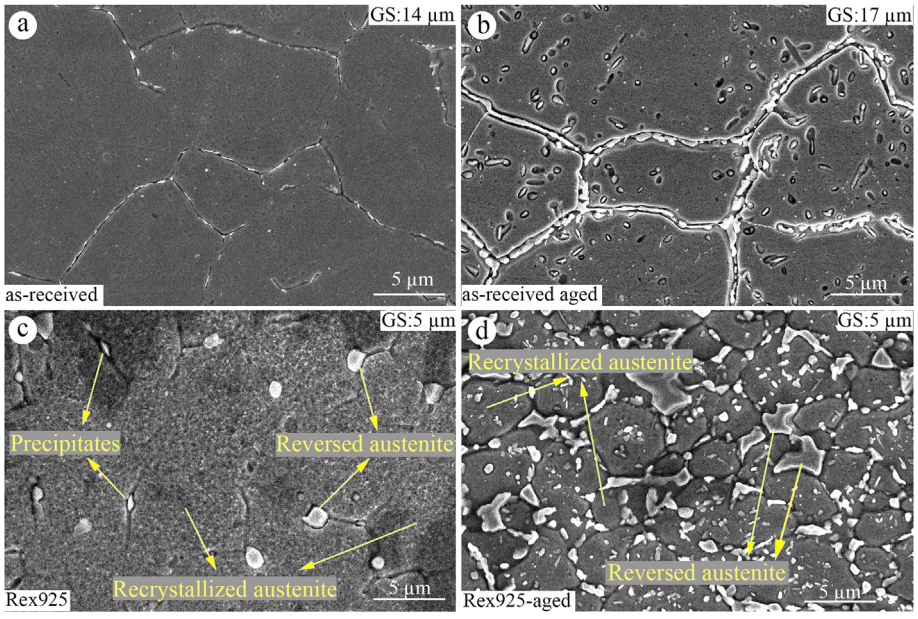

Fig. 5 – SEM micrograph of the (a) as-received, (b) as-received aged, (c) Rex925, and (d) Rex925-aged samples. GS: mean grain size.

Moreover, the average grain size remained close to 5 μm even after aging for the Rex925-aged sample.

The XRD diffractograms of the specimens at different stages of the PDA process are shown in Fig. 6a. The volume fractions of α′-martensite and ε-martensite were calculated according to the method provided in Ref. [39], and the results are illustrated in Fig. 6b. Because the as-received specimen was fully austenitic, both ε-martensite and α′-martensite could form in the microstructure by cold working or aging. However, more formation of α′-martensite occurred owing to cold working, and ε-martensite was more likely to be induced by aging. The peak splitting of the XRD analysis for the Rex925-aged sample could be related to the presence of precipitates, SFs, and ε-martensite, which reduces the microstructural symmetry [40] (see the TEM results in section 3.3).

After the cold-worked specimens were annealed at 530, 630, and 750 °C for 2 h, the volume fraction of α′-martensite decreased and eventually reached zero by increasing the annealing temperature, but the volume fraction of ε-martensite increased to 18% at 750 °C. Recrystallization at 925 °C increased the amount of ε-martensite to 14 vol%, while the amount of α′-martensite decreased to 7.9 vol% compared with that of the cold-worked sample. Interestingly, the aging of the Rex925 specimen caused a sharp increase in the volume fraction of ε-martensite to nearly 43%, whereas α′-martensite disappeared in the Rex925-aged specimen.

The measured lattice parameters of austenite and martensite are listed in Table 2. The austenite lattice parameter was determined using the (111) peak, which corresponds to the value calculated in previous studies [37]. The lattice parameter of α′-martensite was determined from the (211) peak. The parameters *a* and *c* for ε-martensite were determined from the $(10\bar{1}0)$ and (0002) peaks, respectively. The relative length change of the cold-worked sample after annealing at 750 °C for 2 h was calculated using Equation (1) [41], where $\Delta l/l_0$, V, and V_0 are the relative length change, volume, and initial volume, respectively. According to the results shown in Fig. 6b, the thermal treatment changed the volume fraction of phase components from 15% α′-martensite, 7% ε-martensite, and 78% γ-austenite to 18% ε-martensite and 82% γ-austenite. The calculated relative length change was close to the value measured by the dilatometry test. The observed 20% disparity is because of a difference in the heat treatment history, not considering precipitation reactions in the calculations, and the standard error of measurement of phase fractions by XRD testing.

$$\Delta l / l_0 = (1/3).(V - V_0)/V_0 \quad (1)$$

3.2. Mechanical characteristics

A schematic view of the stress-strain curve for the FeMnSi-SMA after loading–unloading is shown in Fig. 7. During loading, the nonlinear deformation behavior after the elastic deformation is due to the austenite-to-martensite transformation followed by the plastic deformation of austenite by dislocation slip along with the martensitic transformation. During unloading, the strain deviates from the linear elastic behavior, which represents the PE (ε_{pse}), and ε_{res} indicates the residual strain. For this particular alloy, it has been shown by Lee et al. [42] that a 0.1% offset yield stress is better suited to

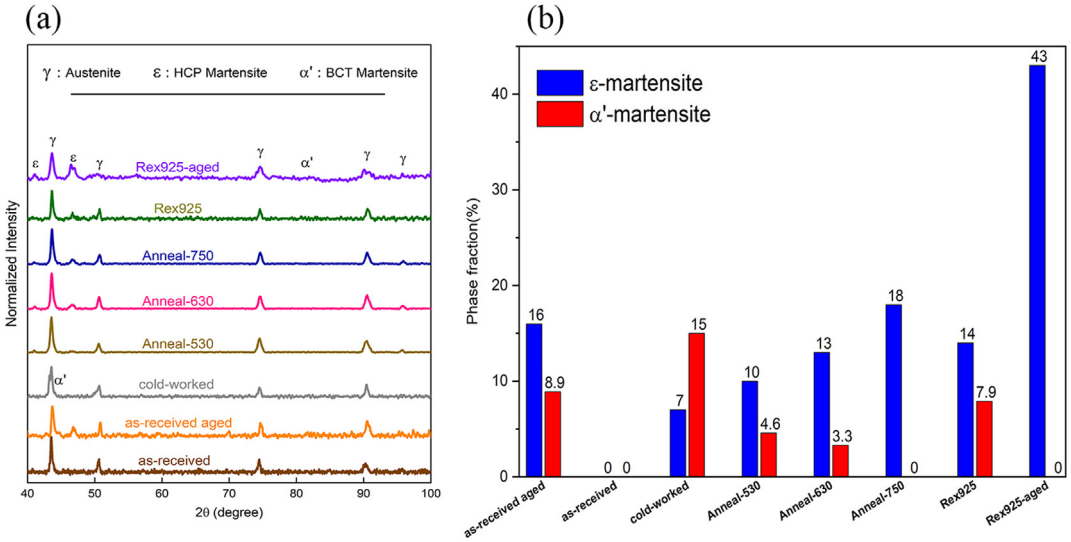

Fig. 6 – (a) XRD diffractograms of the as-received, as-received aged, and PDA-treated specimens. (b) The calculated volume fractions of α′-martensite and ε-martensite corresponding to the XRD results in (a).

Table 2 – Lattice parameters calculated based on the XRD analysis, and relative length changes ($\Delta l/l_0$) resulting from the microstructural evolution during annealing of the cold-worked sample at 750 °C for 2 h.

a (γ) (Å)	*a* (ε-martensite) (Å)	*c* (ε-martensite) (Å)	*a* (α′-martensite) (Å)	$\Delta l/l_0$ (calculated)	$\Delta l/l_0$ (dilatometry)
3.594	2.532	4.280	2.910	−0.00217	−0.00274

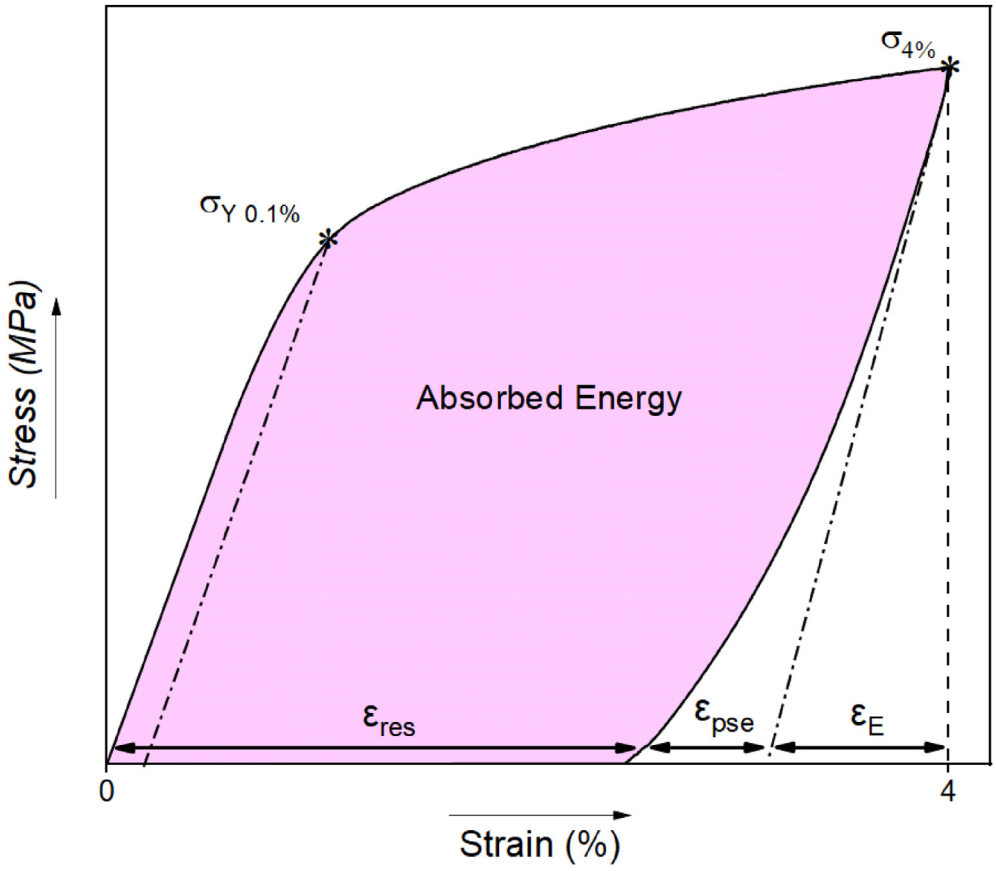

Fig. 7 – Schematic view of a loading–unloading curve for the FeMnSi-SMA strained to 4% in tension, where $\sigma_{4\%}$, $\sigma_{Y\ 0.1\%}$, ε_{pse}, ε_{res}, and ε_E are strength at 4% strain, 0.1% offset yield stress, pseudoelastic strain, residual strain, and elastic strain, respectively.

estimate the onset stress for martensitic transformation than a 0.2% offset yield stress. Therefore, the 0.1% offset yield stress ($\sigma_{Y\ 0.1\%}$) was used in this study. The pseudoelastic strain was calculated according to Equation (2) based on a modulus of elasticity (E) in unloading ($E_{Unloading}$). It should be pointed out that our results are not comparable to those of the other studies [17] where a constant E value of 200 GPa is assumed despite its variations under different microstructural conditions.

The tensile test results for the as-received, as-received aged, Rex925, and Rex925-aged samples are shown in Fig. 8. The values of PE and other mechanical properties of the samples inferred from Fig. 8 are summarized in Table 3. According to Bebling et al. [43], the elastic modulus of this alloy can vary between 40 and 170 GPa under different conditions. The as-received sample exhibited an elastic modulus of 160 GPa, which decreased owing to recrystallization and aging and reached 105 GPa for the Rex925-aged sample. The 0.1% offset yield stress of the as-received sample was 375 MPa. For the as-received aged sample, the yield stress decreased by 100 MPa compared with the as-received sample, but it increased to 555 MPa for the Rex925-aged sample as could be predicted according to the Hall–Petch relationship and uniform precipitate distribution in the microstructure. The strain hardening exponent (n) of the as-received specimen was calculated to be 0.11, which was the lowest among the other conditions, and increased as the thermomechanical treatments were imposed. The maximum value of 'n' belonged to the as-received aged sample with a value of approximately 0.21. The flow stress increased owing to the applied strain for all samples. The strength at 4% strain ($\sigma_{4\%}$) was 600 MPa for both the as-received and as-received aged samples, which was further increased by the applied PDA and reached 775 MPa for the Rex925-aged sample. The PE strain is inversely related to the residual strain. The PE strain for the as-received sample was 0.29%, while it increased to 0.54 after the aging process. A comparison with the as-received sample indicated that the PE strain for the Rex925 sample increased to 0.45% by cold rolling and recrystallization annealing. The PE strain and residual strain obtained for the Rex925-aged sample were 0.63% and 2.85%, respectively. Furthermore, the amount of absorbed energy in the as-received sample was 19.3 J/cm^3, which decreased to 17.0 J/cm^3 with aging but increased to a maximum of 22.0 J/cm^3 for the Rex925-aged sample.

$$\varepsilon_{pse} = 0.04 - \frac{\sigma_{4\%}}{E_{Unloading}} - \varepsilon_{res} \quad (2)$$

3.3. *TEM observations of precipitates and stacking faults*

Fig. 9 shows TEM and HR-TEM images of the Rex925 sample. In Fig. 9a, the dashed white circle indicates a part of the twins with the (111) plane of austenite as the twin plane according to

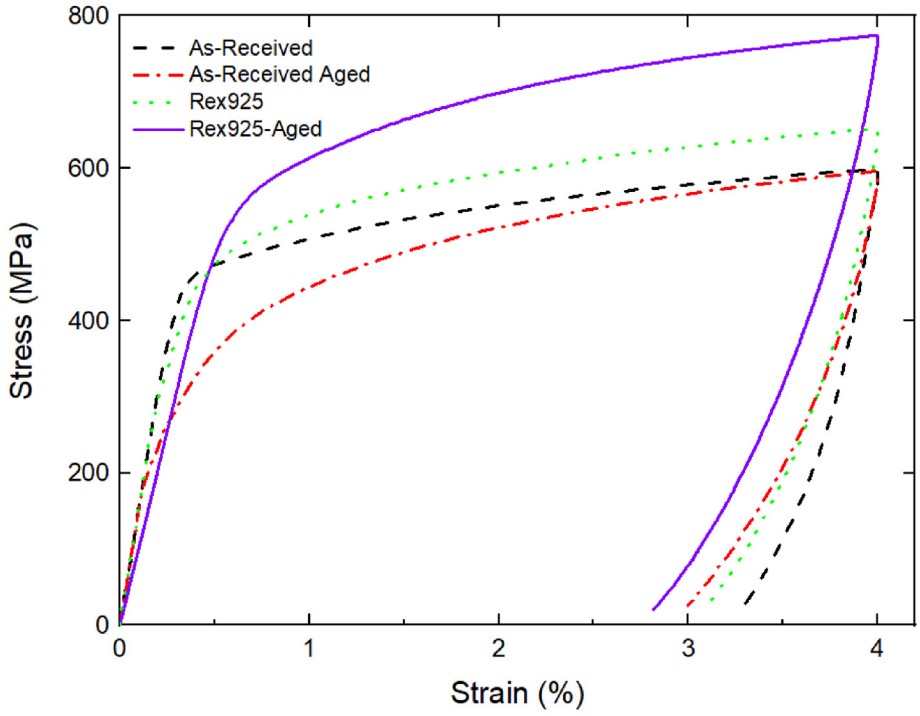

Fig. 8 – Loading–unloading curves of the as-received, as-received aged, Rex925, and Rex925-aged samples strained to 4% in tension.

the selected area electron diffraction (SAED) pattern (inset). Particles with sizes between 180 and 380 nm were located in the austenite matrix. More spherical precipitates are visible in Fig. 9b next to a 1.2 μm polyhedral precipitate at the austenite grain boundary. A dark-field TEM image of the polyhedral precipitate (obtained from the indicated reflection in the SAED pattern) is also shown in Fig. 9b. The TEM-EDS analysis showed that the polyhedral precipitate was a non-carbide rich in Fe, Cr, Mn, and V, but the spherical precipitates were Fe–Cr–Mn–V-rich carbides. According to the shape and chemical composition of the polyhedral-shaped precipitates, these precipitates were considered to be the same as the precipitates in the grain boundary of the as-received sample that enlarged during annealing at 925 °C. Fig. 9c illustrates fine particles of nearly 20 nm in diameter distributed in the austenite matrix. As indicated by the EDS map and HR-TEM image, the revealed fringes were rich in vanadium that could be considered as embryos for the vanadium-rich precipitates. In addition to Si-poor precipitates, Si-containing precipitates with a small amount of carbon (~2 wt.%) were present in the microstructure as shown in Fig. 9d. These precipitates were observed at a dislocation in the austenite phase. An SAED pattern and a dark-field TEM image from one of the precipitates are shown as insets in Fig. 9d.

The TEM image of the Rex925-aged sample is shown in Fig. 10a, indicating a sharp increase in the number of SFs after aging as compared with the Rex925 sample (Fig. 9c). The large number of SFs was consistent with the XRD analysis results, which showed a large amount of ε-martensite in the microstructure. According to Kajiwara's proposed model [44,45], SFs act as nucleation sites for ε-martensite, and the presence of a large number of SFs owing to lattice strain leads to ε-martensite formation to compensate for the lattice distortion induced by the formation of other ε-martensite laths or precipitates. These SFs were formed in specific directions and were limited to the grain boundaries. As a result of aging, various precipitates were formed in the microstructure as shown in Fig. 10b. The TEM-EDS analysis showed that these polyhedral precipitates were carbides rich in Cr, Mn, and V with a much higher carbon content than those observed in the

Table 3 – Characteristics of loading–unloading mechanical properties of the as-received, as-received aged, Rex925, and Rex925-aged samples strained to 4% in tension.

Sample name	$E_{Loading}$ (GPa)	$\sigma_{Y0.1\%}$ (MPa)	n	$\sigma_{4\%}$ (MPa)	$E_{Unloading}$ (GPa)	ε_{pse} (%)	ε_{res} (%)	Absorbed energy (J/cm^3)
As-received	160	375	0.11	600	145	0.29	3.3	19.3
As-received aged	160	275	0.21	600	130	0.54	3	17
Rex925	160	440	0.14	650	145	0.45	3.1	20
Rex925-aged	105	555	0.17	775	150	0.63	2.85	22

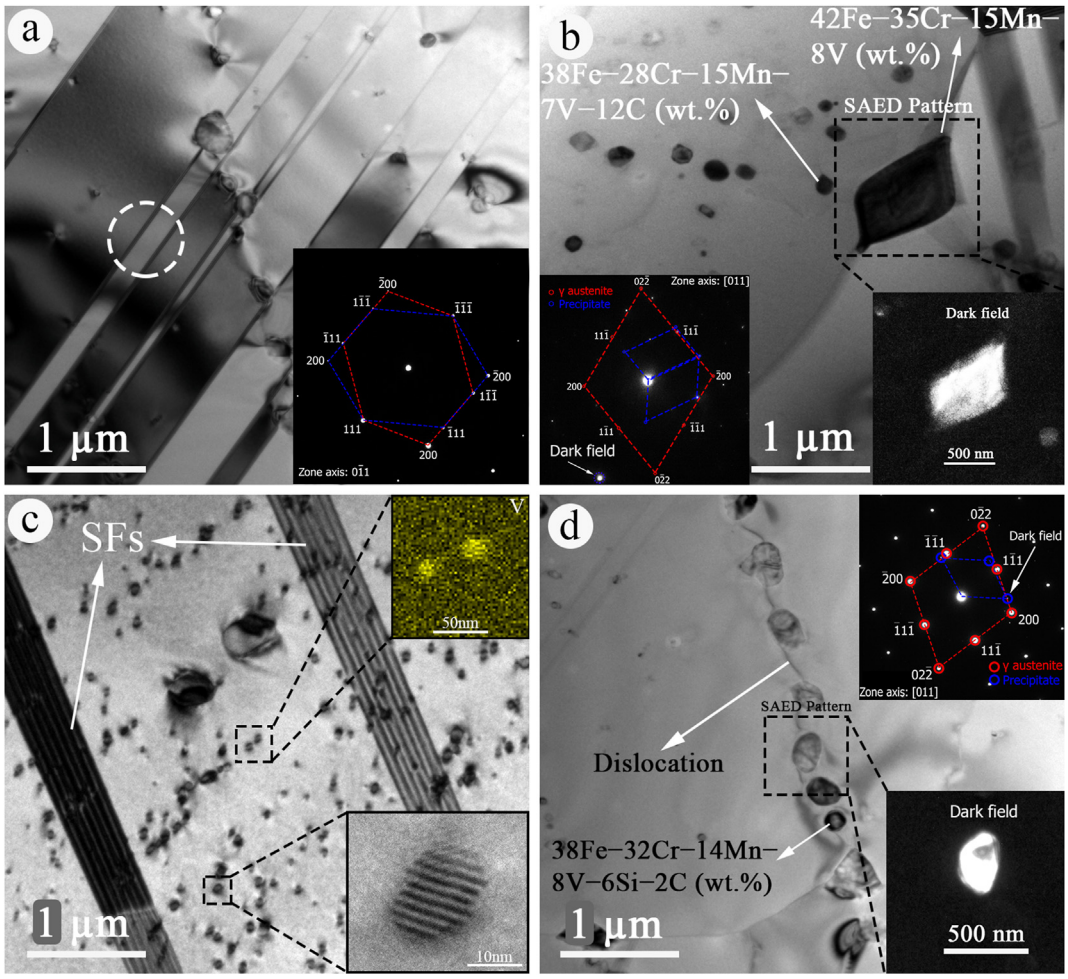

Fig. 9 – (a) Bright-field TEM image of the Rex925 sample and the corresponding SAED pattern of recrystallization twins from the area enclosed by the dashed white circle, and (b) carbides and non-carbide precipitates in the austenite constituent; the insets show the corresponding SAED pattern of the precipitate from the area enclosed by the dashed black square and the dark-field TEM image of the precipitate produced from the indicated reflection. (c) Bright-field TEM image of SFs along with HR-TEM image and EDS map of dark particles as insets. (d) Bright-field TEM image of Si-containing precipitates; the insets represent the SAED pattern of the precipitate from the marked area and a typical dark-field image of the precipitate obtained from the indicated reflection in the diffraction pattern.

Rex925 sample (Fig. 9d). An HR-TEM image of a fine precipitate in the Rex925-aged sample is shown in Fig. 10c. The inverse fast Fourier transform (IFFT) image of the (220) plane of austenite (from the indicated region by the dashed yellow square) confirmed that the precipitate had a semi-coherent interface with the FCC matrix. Additionally, the FFT image of the precipitate indicated double diffraction spots (Fig. 10d). The double diffraction phenomenon occurs when the diffracted beams formed inside the crystalline specimen act as the incident beams for further diffraction by the crystal [46]. In addition, the IFFT image of the entire diffracting planes of the precipitate depicted that colonies of atoms inside the precipitate were arranged in domains with different orientations to accommodate the strain energy to have a semi-coherent interface with the matrix (Fig. 10e). It could be concluded that the relative alignment of several ordered clusters of atoms in the precipitate with respect to the incident electron beam might intensify the double diffraction. The HR-TEM image of an SF line and the IFFT image of a portion of the SF (indicated by the dashed yellow square) are shown in Fig. 10f, indicating that the atomic planes inside the SF were displaced by one atomic layer distance resulting in the formation of ε-martensite (shown with red lines in the inset).

4. Discussion

Equation (3) shows the relationship between the applied strain during the tensile test (ε_{total}) and the residual strain, PE strain, and elastic strain. The elastic strain can be rewritten using Hooke's law. Because the left side of the equation is constant ($\varepsilon_{total} = 4\%$), $\sigma_{4\%}$ must be increased or E should be

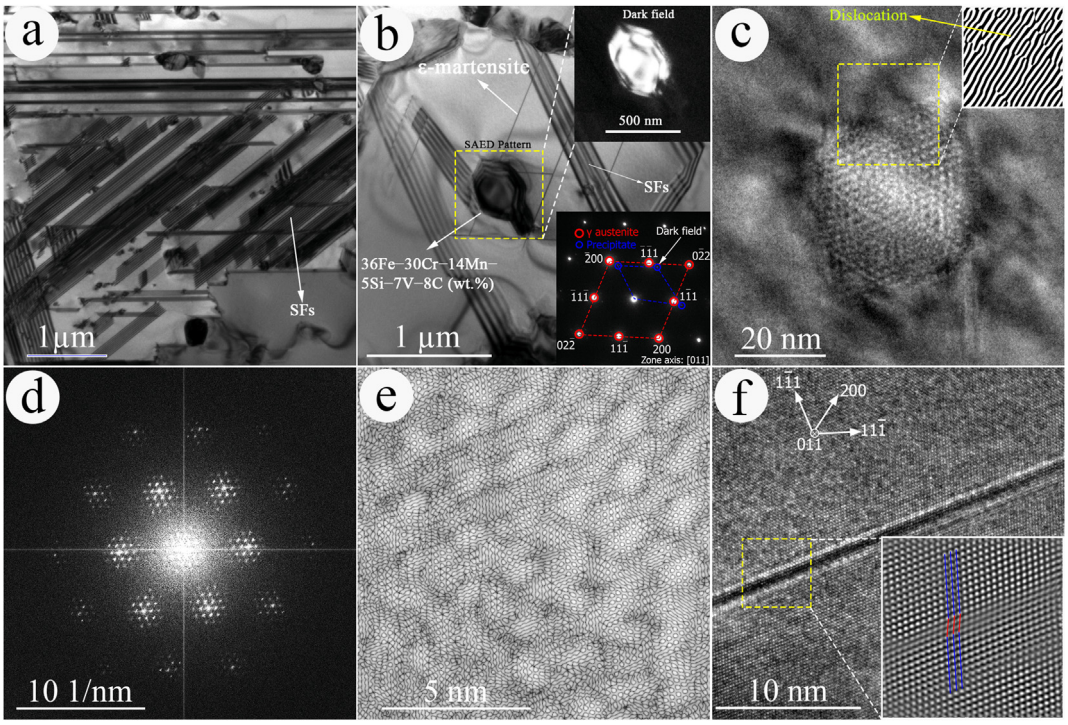

Fig. 10 – (a) Bright-field TEM image of the Rex925-aged sample. (b) A precipitate inside the austenite grain with SFs and ε-martensite laths around it; the insets show the corresponding SAED pattern of the precipitate from the area enclosed by the dashed yellow square and the dark-field TEM image of the precipitate obtained from the indicated reflection. (c) HR-TEM image of a fine, semi-coherent precipitate; the inset shows IFFT of (220) plane of austenite from the area enclosed by the dashed yellow square. (d) FFT image from the precipitate in (c), and (e) corresponding IFFT considering the entire diffracting planes in (d). (f) HR-TEM image and corresponding IFFT (inset) from ε-martensite.

decreased to reduce the amount of residual strain (ε_{res}). In addition, the strain reversibility from the martensite phase to the austenite phase (PE) is another variable that may increase, leading to a reduction in ε_{res}.

$$\varepsilon_{total} = \varepsilon_{res} + \varepsilon_{pse} + \varepsilon_E = \varepsilon_{res} + \varepsilon_{pse} + \frac{\sigma_{4\%}}{E_{Unloading}} \quad (3)$$

4.1. *Effect of aging on the microstructure and pseudoelasticity of the as-received sample*

The as-received sample exhibits equiaxed austenite grains with an average size of 14 μm (Fig. 3a). The as-received alloy is generally used for construction applications after solution annealing at 1100 °C and aging at 830 °C for 2 h [17]. It has recently been observed that aging the as-received alloy at 750 °C for 6 h is a more suitable processing route to improve the PE than aging at 830 °C for 2 h, which is generally conducted on the alloy [47]. The OM images show that aging of the as-received sample leads to a slight increase in the average grain size (Fig. 3b). The FE-SEM images show that polygonal- and rod-shaped precipitates with sizes of 200–700 nm are formed in the microstructure after aging (Fig. 5b). Lai et al. [37] have reported that the formation of these precipitates in the microstructure induces lattice distortion, which in turn induces dislocations and SFs in the microstructure, finally leading to the formation of ε-martensite laths. This observation is consistent with the results of this study; after aging of the as-received sample, the volume fraction of ε-martensite increases to 16 vol% along with 8.9 vol% of α′-martensite (Fig. 6b). According to Bracke et al. [48], α′-martensite can nucleate at the intersection of two ε-martensite laths. The tensile test demonstrates that the elastic modulus remains unchanged owing to precipitation, but the yield strength decreases by 100 MPa after aging of the as-received sample (Fig. 8 and Table 3). Tensile yielding in these alloys is a result of the martensitic transformation which is encouraged by the presence of precipitates in the microstructure. Hence, the reduction in the yield strength is due to precipitate formation and the promotion of martensitic transformation. Although the yield strength of the as-received aged sample is 100 MPa lower than that of the as-received sample, the $\sigma_{4\%}$ values are the same for both. The as-received aged sample compensates for this difference by its higher strain hardening rate (0.21 vs. 0.11). The higher strain-hardening rate in the as-received aged sample is related to the sharp increase in the dislocation density and ε-martensite volume fraction resulting from the aging process [37]. Despite the same $\sigma_{4\%}$, the residual strain (ε_{res}) of the as-received aged sample is 0.3% less than that of the as-received sample. According to Equation (2), the residual strain reduction is due to the improvement in reversibility of the $\gamma \rightarrow \varepsilon$ phase transformation. Lai et al. [37] have observed that the promotion of reversibility by aging is caused by the formation of very thin (less than 3 nm), single-variant ε-martensite laths induced by

lattice strains around precipitates, in contrast to the very thick, multi-variant ε-martensite plates that exist in the precipitate-free microstructure. Furthermore, despite the same $\sigma_{4\%}$, because of the lower yield strength of the as-received aged sample, the amount of absorbed energy reduces by 12% compared with that of the as-received sample.

4.2. *Microstructure and pseudoelasticity evolution during post-deformation annealing*

Generally, the following three microstructural phenomena are likely to occur due to the annealing of cold-worked austenitic steels [49,50]:

1) Strain-induced martensite transforms into ultrafine-grained austenite (reversed austenite).
2) Cold-deformed austenite grains recrystallize into micrometer-sized austenite grains (recrystallized austenite).
3) Reversed and recrystallized austenite grains start growing.

According to the XRD analysis, strain-induced martensite is formed by cold working, which has already been reported elsewhere [42]. The microstructure of the cold-worked sample consists of 15 vol% α′-martensite and 7 vol% ε-martensite. Because of the presence of precipitates at the grain boundaries and triple junctions, as well as the fact that precipitates reduce the critical resolved shear stress (CRSS) for the FCC → HCP phase transformation in this alloy [51], the formation of martensite laths is more concentrated in the areas close to the grain boundaries and triple junctions of the austenite phase.

The cold-worked sample in the dilatometry analysis exhibits a nonlinear length change in the temperature range of 505–750 °C (Fig. 2). The OM images of the samples heat-treated at 530 °C, 630 °C, and 750 °C for 2 h show that annealing at these temperatures does not lead to recrystallization, and the microstructure includes many tangled lines (Fig. 3d–f). The XRD analysis reveals that the amount of α′-martensite decreases after annealing in this temperature range, whereas the number of ε-martensite increases (Fig. 6). For the sample annealed at 750 °C, α′-martensite shows no peaks; and instead, the microstructure contains 18 vol% ε-martensite. According to the research of Lee et al. [52], during continuous heating of the cold-worked sample, α′-martensite transforms into lath-shaped austenite with non-diffusional transformation mechanism and forms subgrain boundaries that are partly represented as the tangled lines seen in the OM images. Another reason for the existence of the tangled lines can be related to the formation of annealing twins and shear bands. The increase in the number of ε-martensite laths with increasing annealing temperature can partly be due to the thermal strain caused by the cooling process [53], which also increases with increasing temperature. Additionally, the precipitation of carbides, which creates a heterogeneous stress distribution within the microstructure, can encourage the formation of ε-martensite [51]. Increasing the annealing temperature to 750 °C increases the volume fraction of carbides and, consequently, induces lattice strains and eventually leads to increased ε-martensite formation. The calculated relative length change for the cold-worked sample after annealing at 750 °C is equal to −0.00217 (Equation (1) and Table 2). This value is caused by the change in the phase fractions from 15 vol% α′-martensite, 7 vol% ε-martensite, and austenite to a microstructure containing 18% ε-martensite and austenite. The calculated value corresponds to the value measured by the dilatometry analysis (−0.00274), which indicates that the relative length change is due to the transformation of α′-martensite to austenite and an increase in the ε-martensite volume fraction.

The OM image of the sample annealed at 925 °C for 50 min shows recrystallized, equiaxed grains with a diameter of approximately 5 μm replacing the deformed grains (Fig. 4a). Additionally, the FE-SEM image of this sample indicates small bright austenite grains (1.2 μm) in the triple junctions next to the 5 μm equiaxed austenite grains (Fig. 5c). Twins are also seen inside the austenite grains in the TEM images of the Rex925 sample (Fig. 9a). Considering the morphology of the observed twins and also the thermomechanical history of the Rex925 sample, these twinned crystals cannot be formed mechanically. According to the study by Bozzolo et al. [54], these are recrystallization twins, which are a subset of annealing twins formed during recrystallization of FCC metals and alloys. Such a twinning mechanism has also been identified in FeMnSiCrNi SMAs [55–57].

As revealed by the TEM investigations in this study, precipitates with less than 1 μm diameter can form in the austenite matrix and its grain boundaries (Fig. 9). Particularly, the TEM-EDS analysis of the dark spots (Fig. 9c) depicts them as vanadium-rich particles. As mentioned previously, these vanadium-rich particles can be considered as embryos for vanadium-rich precipitates. The ellipsoidal morphology of a particle bears an optimum shape to minimize coherent interface energy. In practice, the equilibrium shape of the particles is determined when the following equation is satisfied [58]:

$$\Sigma A_i \gamma_i + \Delta G_s = minimum \tag{4}$$

where A_i is the particle surface area, γ_i is the particle/matrix interfacial energy, and ΔG_s is the elastic strain energy. An oval shape without any sharp corners (which cause high stress concentration fields) with a low ratio of surface area to volume is the optimum shape to satisfy Equation (4). Additionally, as a result of minimizing the particle stain energy, lattice fringes can form during the accommodation of lattice strains within the matrix due to the entry of larger atoms (e.g., vanadium) into the matrix (Fig. 9c).

Owing to the higher 'n' value of the Rex925 sample compared with that of the as-received sample, it is expected that the difference of $\sigma_{4\%}$ between the two samples (50 MPa) would be higher than their yield strength difference (65 MPa); however, this is not the case (Fig. 8 and Table 3). This discrepancy can be explained by the stress-strain curve of the Rex925 sample, which becomes nonlinear at a much lower stress (320 MPa) than the 0.1% offset yield strength of the as-received sample (440 MPa). By considering only Equation (3) and the $\sigma_{4\%}$ difference between the two specimens, a 0.034% PE strain improvement in the Rex925 sample is expected, while the results show an improvement of approximately 0.16%. This may indicate more transformation of austenite to

ε-martensite and vice versa during the loading–unloading tests, which can partly be related to the higher mobility of Shockley partial dislocations in the Rex925 sample compared with the as-received sample.

Unlike the as-received aged sample, the precipitates are uniformly distributed inside the austenite grains of the Rex925-aged sample. Fig. 6b shows that the Rex925 sample consists of approximately 14 vol% ε-martensite and 8 vol% α′-martensite, while the latter martensite fades and the former one increases to approximately 43% after aging. The α′-martensite interfaces in the Rex925 sample likely act as nucleation sites for precipitation, leading to a more uniform particle distribution. The sharp increase in the volume fraction of ε-martensite can be attributed to semi-coherent particle/matrix interfaces that introduce lattice strains in the austenitic matrix (Fig. 10c), leading to strain-induced martensitic transformation.

Despite the formation of a significant amount of ε-martensite in the Rex925-aged sample, α′-martensite, which is known to form as a result of ε-martensite intersection, is not observed. As reported by Pan et al. [59], reducing the average grain size increases the austenite phase strength, resulting in the prevention of ε-martensite formation along different orientations within the austenite grain. This condition reduces the probability of the intersection of ε-martensite laths with each other and subsequent α′-martensite formation.

The tensile test reveals that the Young's modulus of the Rex925-aged sample is reduced by nearly 34% compared with that of the as-received sample. The decrease in the Young's modulus may be due to the large number of SFs in the austenite matrix (Fig. 10a). Moreover, the presence of precipitates in the matrix along with SFs leads to an increase in the dislocation density in the microstructure. The reduction in Young's modulus is attributed to the change in the interatomic bonding configuration at the SFs and additional dislocation motion [60,61].

Finally, the reason for the lowest residual strain value (2.85%) in the Rex925-aged sample can be well interpreted and summarized by means of Fig. 11. The figure shows that by microstructural engineering through cold working process, annealing, and controlled precipitation, a microstructure composed of fine austenite grains, SFs, precipitates, and thin ε-martensite laths accompanied by partial dislocation arrays is evolved which eventually leads to PE improvement. In fact, the microstructural engineering facilitates the $\gamma \rightleftharpoons \varepsilon$ transformation during loading–unloading which is shown by the reduction of the Young's modulus and the increase in $\sigma_{4\%}$. Also, an increase of 30% in the absorbed energy during loading–unloading compared with that of the as-received aged sample makes this modified microstructure more suitable for civil engineering applications, particularly for manufacturing dampers and energy dissipation structures.

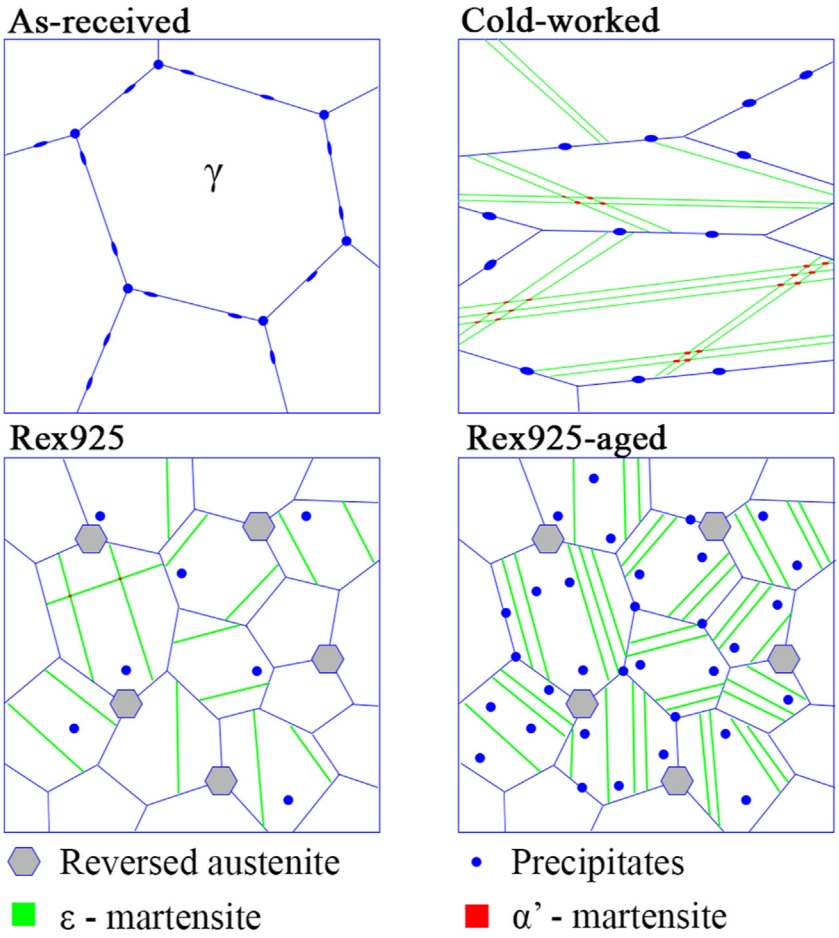

Fig. 11 – Schematic view of the microstructural evolution during post-deformation annealing.

Although it is possible to increase the absorbed energy by enhancing the flow stress level, a reduction in the residual strain leads to a lower value of the absorbed energy. Hence, the achievement of this study is the reduction of the residual strain and increasing the absorbed energy simultaneously.

5. Conclusions

This study provides a new understanding of the most important mechanisms that influence the pseudoelastic behavior of an FeMnSi-based shape memory alloy (SMA) that can be further used to control and improve the mechanical performance of the alloy. The effects of recrystallization parameters (temperature and time) and aging on the microstructural evolution and mechanical properties of the Fe–17Mn–5Si–10Cr–4Ni–1(V–C) (wt.%) SMA have been investigated. Based on experimental investigations and detailed microstructural and mechanical analyses, the following conclusions can be drawn:

1. Annealing the cold-worked samples in the temperature range of 530–750 °C does not lead to recrystallization. With increasing the annealing temperature in this range, the microstructural analysis reveals that α'-martensite transforms to austenite (γ), and the volume fraction of ε-martensite increases.
2. Annealing the cold-worked sample at 925 °C for 50 min and subsequent aging at 750 °C for 6 h (named as Rex925-aged condition) result in a microstructure consisting of recrystallized, equiaxed austenite grains with an average size of 5 μm and reversed austenite grains of 1–2 μm in triple junctions of the recrystallized matrix. The uniform distribution of precipitates leads to the formation of a high density of SFs and ε-martensite laths in the microstructure.
3. Microstructural engineering through cold working, annealing, and controlled precipitation in the FeMnSi-based SMA is employed to obtain a microstructure composed of fine austenite grains, SFs, precipitates, thin ε-martensite laths accompanied by partial dislocation arrays. In comparison to the as-received microstructure, the engineered microstructure of the Rex925-aged sample results in a decrease in Young's modulus and an increase in the $\sigma_{4\%}$ owing to facilitating the $\gamma \rightleftharpoons \varepsilon$ transformation during loading–unloading experiments. These changes eventually lead to a reduction in the residual strain.
4. The absorbed energy attains a value of 22 J/cm^3, a nearly 30% improvement over the as-received aged sample. The reduced amount of the residual strain and increased amount of the absorbed energy of the Rex925-aged sample in comparison to those of the as-received aged sample make this alloy more suitable for seismic damping and recentering applications.

Data availability

The raw/processed data required to reproduce these findings cannot be shared at this time as the data also forms part of an ongoing study.

Declaration of Competing Interest

The authors declare that they have no known competing financial interests or personal relationships that could have appeared to influence the work reported in this paper.

Acknowledgment

The authors acknowledge the support of re-fer AG, Switzerland, for providing the material for this research study.

REFERENCES

[1] Dahake S, Awate N, Shelke R, Khalatkar A. Shape memory alloy as a smart material: a review, vol. 2. Smart Technologies for Energy, Environment and Sustainable Development; 2022. p. 395–401.
[2] Hartl DJ, Lagoudas DC. Aerospace applications of shape memory alloys. Proc IME G J Aero Eng 2007;221(4):535–52.
[3] Machado L, Savi M. Medical applications of shape memory alloys. Braz J Med Biol Res 2003;36(6):683–91.
[4] Maji AK, Negret I. Smart prestressing with shape-memory alloy. J Eng Mech 1998;124(10):1121–8.
[5] Use of shape-memory alloys in construction: a critical reviewChang W-S, Araki Y, editors. Proceedings of the Institution of Civil Engineers-Civil Engineering 2016;169(2):87–95.
[6] Leinenbach C, Kramer H, Bernhard C, Eifler D. Thermo-mechanical properties of an Fe–Mn–Si–Cr–Ni–VC shape memory alloy with low transformation temperature. Adv Eng Mater 2012;14(1):62–7. 2.
[7] Moriya Y, Kimura H, Ishizaki S, Hashizume S, Suzuki S, Suzuki H, et al. Properties of Fe-Cr-Ni-Mn-Si (-Co) shape memory alloys. J Phys IV 1991;1(C4). C4-433-C4-7.
[8] Otsuka K, Wayman CM. Shape memory materials. Cambridge university press; 1999.
[9] Gu X-L, Chen Z-Y, Yu Q-Q, Ghafoori E. Stress recovery behavior of an Fe-Mn-Si shape memory alloy. Eng Struct 2021;243:112710.
[10] Lagoudas DC. Shape memory alloys: modeling and engineering applications. Springer; 2008.
[11] Janke L, Czaderski C, Motavalli M, Ruth J. Applications of shape memory alloys in civil engineering structures—overview, limits and new ideas. Mater Struct 2005;38(5):578–92.
[12] Choi E, Chung Y-S, Choi J-H, Kim H-T, Lee H. The confining effectiveness of NiTiNb and NiTi SMA wire jackets for concrete. Smart Mater Struct 2010;19(3):035024.
[13] Hsu T, Zuyao X. Martensitic transformation in Fe-Mn-Si based alloys. Mater Sci Eng, A 1999;273:494–7.
[14] Otsuka H, Nakajima K, Maruyama T. Superelastic behavior of Fe–Mn–Si–Cr shape memory alloy coil. Mater Trans, JIM 2000;41(4):547–9.
[15] Sato A, Chishima E, Soma K, Mori T. Shape memory effect in $\gamma \rightleftarrows \varepsilon$ transformation in Fe-30Mn-1Si alloy single crystals. Acta Metall 1982;30(6):1177–83.
[16] Talonen J, Hänninen H. Formation of shear bands and strain-induced martensite during plastic deformation of metastable austenitic stainless steels. Acta Mater 2007;55(18):6108–18.
[17] Arabi-Hashemi A, Lee W, Leinenbach C. Recovery stress formation in FeMnSi based shape memory alloys: impact of

precipitates, texture and grain size. Mater Des 2018;139:258–68.
[18] Rahman K, Vorontsov V, Dye D. The effect of grain size on the twin initiation stress in a TWIP steel. Acta Mater 2015;89:247–57.
[19] Sawaguchi T, Kikuchi T, Kajiwara S. The pseudoelastic behavior of Fe–Mn–Si-based shape memory alloys containing Nb and C. Smart Mater Struct 2005;14(5):S317–22.
[20] Kaiiwara S, Liu D, Kikuchi T, Shinya N. Remarkable improvement of shape memory effect in Fe-Mn-Si based shape memory alloys by producing NbC precipitates. Scripta Mater 2001;44(12):2809–14.
[21] Farjami S, Hiraga K, Kubo H. Shape memory effect and crystallographic investigation in VN containing Fe-Mn-Si-Cr Alloys. Mater Trans 2004;45(3):930–5.
[22] Vůjtěch J, Ryjáček P, Matos JC, Ghafoori E. Iron-Based shape memory alloy for strengthening of 113-Year bridge. Eng Struct 2021;248:113231.
[23] Fosdick R, Ketema Y. Shape memory alloys for passive vibration damping. J Intell Mater Syst Struct 1998;9(10):854–70.
[24] Hosseini E, Ghafoori E, Leinenbach C, Motavalli M, Holdsworth SR. Stress recovery and cyclic behaviour of an Fe–Mn–Si shape memory alloy after multiple thermal activation. Smart Mater Struct 2018;27:025009.
[25] Yang Y, Arabi-Hashemi A, Leinenbach C, Shahverdi M. Influence of thermal treatment conditions on recovery stress formation in an FeMnSi-SMA. Mater Sci Eng, A 2021;802:140694.
[26] Rosa DIH, Hartloper A, de Castro e Sousa A, Lignos DG, Motavalli M, Ghafoori E. Experimental behavior of iron-based shape memory alloys under cyclic loading histories. Construct Build Mater 2021;272:121712.
[27] Ghafoori E, Hosseini E, Leinenbach C, Michels J, Motavalli M. Fatigue behavior of a Fe-Mn-Si shape memory alloy used for prestressed strengthening. Mater Des 2017;133:349–62.
[28] Ghafoori E, Neuenschwander M, Shahverdi M, Czaderski C, Fontana M. Elevated temperature behavior of an iron-based shape memory alloy used for prestressed strengthening of civil structures. Construct Build Mater 2019;211:437–52.
[29] Wang W, Hosseini A, Ghafoori E. Experimental study on Fe-SMA-to-steel adhesively bonded interfaces using DIC. Eng Fract Mech 2021;244:107553.
[30] Kim D, Ferretto I, Jeon JB, Leinenbach C, Lee W. Formation of metastable bcc-δ phase and its transformation to fcc-γ in laser powder bed fusion of Fe-Mn-Si shape memory alloy. J Mater Res Technol 2021;14:2782–8.
[31] Izadi M, Motavalli M, Ghafoori E. Iron-based shape memory alloy (Fe-SMA) for fatigue strengthening of cracked steel bridge connections. Construct Build Mater 2019;227:116800.
[32] Izadi M, Motavalli M, Ghafoori E. Thermally-activated shape memory alloys for retrofitting bridge double-angle connections. Eng Struct 2021;245:112827.
[33] Izadi M, Ghafoori E, Motavalli M, Maalek S. Iron-based shape memory alloy for the fatigue strengthening of cracked steel plates: effects of re-activations and loading frequencies. Eng Struct 2018;176:953–67.
[34] Izadi M, Ghafoori E, Shahverdi M, Motavalli M, Maalek S. Development of an iron-based shape memory alloy (Fe-SMA) strengthening system for steel plates. Eng Struct 2018;174:433–46.
[35] Wang W, Li L, Hosseini A, Ghafoori E. Novel fatigue strengthening solution for metallic structures using adhesively bonded Fe-SMA strips: a proof of concept study. Int J Fatig 2021;148:106237.
[36] Li J, Zhao M, Jiang Q. Alloy design of FeMnSiCrNi shape-memory alloys related to stacking-fault energy. Metall Mater Trans 2000;31(3):581–4.
[37] Lai M, Li Y, Lillpopp L, Ponge D, Will S, Raabe D. On the origin of the improvement of shape memory effect by precipitating VC in Fe–Mn–Si-based shape memory alloys. Acta Mater 2018;155:222–35.
[38] Nikulin I, Sawaguchi T, Yoshinaka F, Takamori S. Influence of cold rolling deformation mechanisms on the grain refinement of Fe–15Mn–10Cr–8Ni–4Si austenitic alloy. Mater Char 2020;162:110191.
[39] Robertson J. Elements of X-ray diffraction by BD cullity. International Union of Crystallography; 1979.
[40] Warren B. X-Ray diffraction. New York: Dover.; 1990. p. 253.
[41] Volume change associated to carbon partitioning from martensite to austeniteSantofimia M, Zhao L, Sietsma J, editors. Mater Sci Forum 2012:2290–5.
[42] Lee W, Weber B, Feltrin G, Czaderski C, Motavalli M, Leinenbach C. Phase transformation behavior under uniaxial deformation of an Fe–Mn–Si–Cr–Ni–VC shape memory alloy. Mater Sci Eng, A 2013;581:1–7.
[43] Beßling M, Czaderski C, Orlowsky J. Prestressing effect of shape memory alloy reinforcements under serviceability tensile loads. Buildings 2021;11(3):101.
[44] Kajiwara S. Characteristic features of shape memory effect and related transformation behavior in Fe-based alloys. Mater Sci Eng, A 1999;273:67–88.
[45] Bergeon N, Kajiwara S, Kikuchi T. Atomic force microscope study of stress-induced martensite formation and its reverse transformation in a thermomechanically treated Fe–Mn–Si–Cr–Ni alloy. Acta Mater 2000;48(16):4053–64.
[46] Hirsch P, Howie A, Nicholson R, Pashley D, Whelan M. Electron microscopy of thin crystals, vol. 358. London, UK: Butterworths.; 1965.
[47] Mohri M, Ferretto I, Leinenbach C, Kim D, Lignos DG, Ghafoori E. Effect of thermomechanical treatment and microstructure on pseudo-elastic behavior of Fe–Mn–Si–Cr–Ni-(V, C) shape memory alloy. Mater Sci Eng, A 2022;855:143917.
[48] Bracke L, Kestens L, Penning J. Transformation mechanism of α′-martensite in an austenitic Fe–Mn–C–N alloy. Scripta Mater 2007;57(5):385–8.
[49] Koohdar H, Nili-Ahmadabadi M, Habibi-Parsa M, Jafarian H. Development of pseudoelasticity in Fe–10Ni–7Mn (wt%) high strength martensitic steel by intercritical heat treatment and subsequent ageing. Mater Sci Eng, A 2015;621:52–60.
[50] Sohrabi MJ, Naghizadeh M, Mirzadeh H. Deformation-induced martensite in austenitic stainless steels: a review. Arch Civ Mech Eng 2020;20(4):1–24.
[51] Leinenbach C, Arabi-Hashemi A, Lee W, Lis A, Sadegh-Ahmadi M, Van Petegem S, et al. Characterization of the deformation and phase transformation behavior of VC-free and VC-containing FeMnSi-based shape memory alloys by in situ neutron diffraction. Mater Sci Eng, A 2017;703:314–23.
[52] Lee S-J, Park Y-M, Lee Y-K. Reverse transformation mechanism of martensite to austenite in a metastable austenitic alloy. Mater Sci Eng, A 2009;515(1–2):32–7.
[53] Bujoreanu LG, Stanciu S, Comaneci RI, Meyer M, Dia V, Lohan C. Factors influencing the reversion of stress-induced martensite to austenite in a Fe-Mn-Si-Cr-Ni shape memory alloy. J Mater Eng Perform 2009;18(5):500–5.
[54] Bozzolo N, Bernacki M. Viewpoint on the formation and evolution of annealing twins during thermomechanical processing of FCC metals and alloys. Metall Mater Trans 2020;51(6):2665–84.
[55] Jiang S, Wang Y, Zhang Y, Xing X, Yan B. Constitutive behavior and microstructural evolution of FeMnSiCrNi shape memory alloy subjected to compressive deformation at high temperatures. Mater Des 2019;182:108019.

[56] Jiang S, Wang Y, Yan B, Zhang Y. Hot workability of FeMnSiCrNi shape memory alloy based on processing map and martensitic transformation. J Alloys Compd 2019;806:1153–65.
[57] Jiang S, Wang Y, Zhang Y, Xing X. Role of stacking faults in martensite transformation of FeMnSiCrNi shape memory alloy subjected to plastic deformation at high temperatures. Intermetallics 2020;124:106841.
[58] Porter DA, Easterling KE. Phase transformations in metals and alloys (revised reprint). CRC press; 2009.
[59] Pan M-M, Zhang X-M, Zhou D, Misra R, Chen P. Fe–Mn–Si–Cr–Ni based shape memory alloy: thermal and stress-induced martensite. Mater Sci Eng, A 2020;797:140107.
[60] Chen Y, Burgess T, An X, Mai Y-W, Tan HH, Zou J, et al. Effect of a high density of stacking faults on the Young's modulus of GaAs nanowires. Nano Lett 2016;16(3):1911–6.
[61] Over H, Knotek O, Lugscheider E. Elastic properties of silicon single crystals in dependence on temperature and dislocation density. Z Metallkd 1982;73(9):552–7.